Converging shocks in elastic-plastic solids

A. López Ortega, M. Lombardini, and D. J. Hill

Phys. Rev. E **84**, 056307 — Published 14 November 2011

DOI: 10.1103/PhysRevE.84.056307

On converging shocks in elastic–plastic solids

A. López Ortega, M. Lombardini, and D.J. Hill

Graduate Aerospace Laboratories, California Institute of Technology, Pasadena, California 91125, USA

We present an approximate description of the behavior of an elastic–plastic material processed by a cylindrically/spherically symmetric converging shock, following Whitham's shock dynamics theory. Originally applied with success to various gas dynamics problems, this theory is presently derived for solid media, in both elastic and plastic regimes. The exact solutions of the shock dynamics equations obtained reproduce well the results obtained by high-resolution numerical simulations. The examined constitutive laws share a compressible neo-Hookean structure for the internal energy $e = e_s(I_1) + e_h(\rho, \varsigma)$, where e_s accounts for shear through the first invariant of the Cauchy–Green tensor, and e_h represents the hydrostatic contribution as a function of the density ρ and entropy ς. In the strong-shock limit, reached as the shock approaches the axis/origin $r = 0$, we show that compression effects are dominant over shear deformations. For an isothermal constitutive law, i.e. $e_h = e_h(\rho)$, with a power-law dependence $e_h \propto \rho^\alpha$, shock dynamics predicts that for a converging shock located at $r = R(t)$ at time t, the Mach number increases as $M \propto (\log(1/R))^\alpha$, independently of the space index s, where $s = 2$ in cylindrical geometry and 3 in spherical geometry. An alternative isothermal constitutive law with $p(\rho)$ of the Arctanh type, which enforces a finite density in the strong-shock limit, leads to $M \propto R^{-(s-1)}$ for strong shocks. A non-isothermal constitutive law, whose hydrostatic part e_h is that of an ideal gas, is also tested, recovering the strong-shock limit $M \propto R^{-(s-1)/n(\gamma)}$ originally derived by Whitham for perfect gases, where γ is inherently related to the maximum compression ratio that the material can reach, $(\gamma+1)/(\gamma-1)$. From these strong-shock limits, we also estimate analytically the density, radial velocity, pressure and sound speed immediately behind the shock. While the hydrostatic part of the energy essentially commands the strong-shock behavior, the shear modulus and yield stress modify the compression ratio and velocity of the shock far from the axis/origin. A characterization of the elastic–plastic transition in converging shocks, which involves an elastic precursor and a plastic compression region, is finally exposed.

I. INTRODUCTION

Cylindrical and spherical shock waves propagating in solid materials have been recently the focus of attention in applied physics and engineering, starting with the problem of an out-going (exploding) wave forced by a moving cylinder/sphere [1], as occurs in projectile penetration. The particular study of converging shocks in solids is relevant to the production of high temperatures and pressures in condensed matter, with possible applications to inertial confinement fusion [2]. Recent work has actually suggested the utilization of ultra-dense deuterium with density $\approx 140\,\mathrm{kg.cm^{-3}}$ for fusion experiments [3, 4]. However, experimental studies reveal complications inherent to the measurement techniques and the difficulty of producing a quasi-radially symmetric flow with minimal excursions from circularity.

Guderley [5] originally considered cylindrically and spherically symmetric converging shock waves in an inviscid ideal gas and showed that, if the shock wave is initially already strong, there exist similarity solutions in which the radial location $R(t)$ of the shock is proportional to a power of the time measured from the instant when the shock has imploded to $r = 0$. The Guderley implosion problem has been addressed by Whitham's shock dynamics (WSD) theory [6], which gives good approximations to the values of the Guderley exponent. WSD was also extended to imploding shocks initially infinitesimally weak [7] and applied to two-dimensional gas dynamics problems [8] such as shock diffraction by a wedge and shock stability [9].

Yadav & Singh [10] studied the propagation of spherically converging shocks in metals following WSD and employing a Mie–Gruneisen equation of state for the hydrostatic part of the energy but not accounting for the effects of shear. Their solution for the post-shock pressure approaches an inverse power of R, the exponent varying with the effective specific heat ratio of the metal. In that study, a distinction was also made between the behavior of light metals like aluminum, which behave like gases in the strong-shock limit, and heavier materials like copper, which exhibit a slight variation of it. A similar equation of state was used by Hiroe, Matsuo & Fujiwara [11] who simulated a cylindrically imploding shock (and its subsequent reflection off the axis) using a random choice numerical method. They observed that the flow only falls within the self-similar regime commonly observed with gases in extreme proximity of the axis.

We propose the use of hyper-elastic constitutive laws to introduce shear deformations. The laws are formulated in terms of an internal energy that is an explicit function of the material deformation, and from which the stress tensor can be derived in a fashion that results in a conservative hyperbolic system [12]. Among the various constitutive laws of the hyper-elastic type, Miller & Colella [13] proposed an additive decomposition of the internal energy in terms of hydrostatic, thermal and shear parts. Gavrilyuk *et al.* [14] proposed a similar decomposition with an hydrostatic part that imitates a stiffened gas. These constitutive laws, in which the shear part depends on the three invariants of the Cauchy–Green tensor $\mathbf{C}$ and the material properties can vary with the density and entropy, are fairly general and adapt well to different stress conditions. A summary of other constitutive laws specific to high-compression shocks in different media (e.g. porous materials) can be found in [15], with an emphasis on hydrostatic terms of the Mie–Gruneisen type. In our analysis, we examine a compressible neo-Hookean constitutive law [16] with constant material properties and a shear part which is a function of the first invariant of $\mathbf{C}$ only. This rather simple approach reduces the complexity of the problem, allowing us to obtain analytical solutions.

Among important effects not considered here, shock-induced melting must be briefly discussed here. During shock compression, temperature can rise dramatically, but due to corresponding increase in pressure, the solid does not necessarily melt. However, melting can occur during the post-shock release phase. To be more precise, continuously driven shock waves are usually experimentally difficult to maintain. For example, high-velocity flier plate impactors have finite momentum, and high-intensity laser have finite pulse times. The shock driving force ultimately vanishes and a release wave starts propagating behind the compressed material, usually at a faster speed than the shock front. The release is isentropic and reduces the density and pressure while maintaining the temperature, allowing the melting of the material.

To describe the large deformations in a highly compressed material, we first introduce in Section II an Eulerian description of the conservation laws governing the finite-deformation evolution of a purely elastic material under radially symmetric conditions. After describing the general compressible neo-Hookean hyper-elastic constitutive law employed, a WSD analytical solution is constructed and compared against high-resolution numerical simulations. Section III extends the study to finite-deformation plasticity and provides similar comparisons between numerical and analytical results.

II. ELASTIC MOTION

A. Governing equations for radially symmetric motion

We describe here the radially symmetric motion of a continuum elastic medium induced by the collapse of cylindrical and spherical imploding shock waves. In an Eulerian framework, the conservation of mass, momentum and energy take the form

$$\frac{\partial \rho}{\partial t} + u\frac{\partial \rho}{\partial r} + \rho\frac{\partial u}{\partial r} = -(s-1)\frac{\rho u}{r}, \tag{1a}$$

$$\frac{\partial u}{\partial t} + u\frac{\partial u}{\partial r} - \frac{1}{\rho}\frac{\partial \sigma_{rr}}{\partial r} = (s-1)\frac{\sigma_{rr}-\sigma_{\theta\theta}}{\rho r}, \tag{1b}$$

$$\frac{\partial e}{\partial t} + u\frac{\partial e}{\partial r} - \frac{\sigma_{rr}}{\rho}\frac{\partial u}{\partial r} = (s-1)\frac{u\sigma_{\theta\theta}}{\rho r}, \tag{1c}$$

where r is the distance to the axis/origin, ρ the density field, u the radial component of velocity vector, e the internal energy, and s the space index, with $s=1$ for planar symmetry, $s=2$ for cylindrical symmetry and $s=3$ for spherical symmetry. We assume a homogeneous isotropic hyper-elastic material, where e only depends on the three invariants of the Cauchy–Green tensor $\mathbf{C} = \boldsymbol{f}^{-T}\boldsymbol{f}^{-1}$, namely

$$I_1 = \mathrm{tr}(\mathbf{C}), \tag{2a}$$

$$I_2 = \det(\mathbf{C})\mathbf{C}^{-1}, \tag{2b}$$

$$I_3 = \det(\mathbf{C}) = 1/\det(\boldsymbol{f})^2, \tag{2c}$$

and on the specific entropy ς. An analysis of the evolution equation for the internal energy at constant entropy,

$$\frac{De}{Dt} = \frac{\partial e}{\partial f_{ij}}\frac{Df_{ij}}{Dt} = -\frac{\partial e}{\partial f_{ij}} f_{ik}\frac{\partial u_k}{\partial x_j} = \frac{1}{\rho}\sigma_{ij}\frac{\partial u_i}{\partial x_j}, \tag{3}$$

allows us to compute the stresses from e by $= -\rho\boldsymbol{f}^T\partial e/\partial\boldsymbol{f}$. In these definitions, the inverse deformation tensor $\boldsymbol{f}$ represents the gradient of the mapping that transforms Eulerian coordinates to Lagrangian (material) coordinates, and is commonly written in Cartesian coordinates as $f_{ij} = \partial X_i/\partial x_j$.

In cylindrical symmetry ($s=2$), the inverse deformation tensor reduces to a diagonal form $\boldsymbol{f} = \mathrm{diag}(f_{rr}, f_{\theta\theta}, 1)$, where plane strain is assumed (no deformation in the z-direction). Similarly, $\boldsymbol{f} = \mathrm{diag}(f_{rr}, f_{\theta\theta}, f_{\phi\phi})$ for $s=3$. The density constraint $J \equiv \rho_0/\rho = 1/\det\boldsymbol{f}$, where ρ_0 is the density of the undeformed material, reduces the complexity of the problem as the non-radial components of $\boldsymbol{f}$ are functions of f_{rr} and ρ:

$$f_{\theta\theta} = \frac{1}{Jf_{rr}} \quad \text{for } s=2, \tag{4a}$$

$$f_{\theta\theta} = f_{\phi\phi} = \sqrt{\frac{1}{Jf_{rr}}} \quad \text{for } s=3. \tag{4b}$$

At this point, the system of equations (1) can be closed by the choice of a specific constitutive law of the form $e(I_1, I_2, I_3, \varsigma)$, which would then allow us to determine σ_{rr} and $\sigma_{\theta\theta}$ as a function of the inverse deformation tensor components and e. Thanks to (4), only the equation of evolution of the inverse deformation tensor component f_{rr} is then needed to complete (1), given $e(I_1, I_2, I_3, \varsigma)$, and in the same Eulerian formalism,

$$\frac{\partial f_{rr}}{\partial t} + f_{rr}\frac{\partial u}{\partial r} + u\frac{\partial f_{rr}}{\partial r} = 0. \tag{5}$$

B. Numerical method and computational geometry

The equations of motion (1) and (5) can be rewritten in a conservative form and solved using a one-dimensional second-order MUSCL finite volume scheme with a 4th-order Runge–Kutta time-stepping method. At each computational cell interface, a Riemann problem is solved approximately using the HLL method. The geometric source terms are computed by operator splitting, and cell averages are evaluated at the cell centers, which overcomes the singularity at $r = 0$. The simulations were performed in spherical geometry but similar results can be achieved in cylindrical geometry as well. To achieve sufficiently steep capturing of the shock waves, a resolution of 10^4 cells was used. More information about these numerical methods can be found in Chapter 10 (HLL), 14 (MUSCL) and 15 (source terms) of [17]. To investigate the strong-shock limit, additional simulations were performed using adaptive mesh refinement (AMR) as described in [18]. Three levels of refinement, each one increasing resolution by four, over the initial 10^4 cells, were used.

The shock is initiated at the position R_i at the left boundary of the computational domain to avoid the calculation of $f_{\theta\theta}$ at $t = 0$ for all r behind the shock ($f_{\theta\theta} = 0$ immediately behind the shock), and propagates from left to right. The value of the initial radius R_i is not relevant here since the problem does not have a characteristic length scale. The boundary condition at the left-end of the domain is transmissive (zero-gradient boundary condition), while reflective boundary conditions are applied at the axis/origin $r = 0$.

C. Whitham's shock dynamics and Rankine–Hugoniot jump conditions

To apply WSD, the system of PDEs (1) and (5) advecting the vector of primitive variables (ρ, u, e, f_{rr}) can be first decoupled into a set of ordinary differential equations (ODEs) called the 'characteristic' equations as derived in Appendix A. The essential assumption behind the WSD approach is based on the intuition that, as the converging shock is adjusting to changes in the geometry, the shock ignores its interaction with the flow behind it and its motion can be approximated by integrating the equation governing the flow along the $u+a$-characteristics, a being the sound speed. Numerical simulations confirm that the slope of the family of $u + a$-characteristics is indeed close to the slope of a converging shock trajectory, in particular when the shock gets stronger (e.g. see Fig. 1(b)). This intuition can be motivated by a small-perturbation analysis of the shock propagation down a nonuniform shocktube of cross-sectional area $A(r)$ slowly varying from $A(r)$ to $A(r) + \mathrm{d}A$. Over the length of the shocktube, the errors might accumulate but they are neglected in the WSD theory.

Assume that the shock is located at the radial position $r = R(t)$ at time t. For the characteristic curve of slope $u + a$, the ODE relating the changes in the post-shock properties as r ($> R$) varies is further simplified by using the Rankine–Hugoniot (RH) jump conditions across the moving shock, which give the primitive variables immediately behind the shock in terms of the shock Mach number M. In the frame of reference of the shock imploding at the instantaneous speed $U(t) = -\mathrm{d}R/\mathrm{d}t > 0$, the weak formulation of the conservation equations (1) and (5) leads to the following jump conditions normal to the shock,

$$\rho(U - u) = \rho_0 U, \tag{6a}$$

$$\rho(U - u)^2 - \sigma_{rr} = \rho_0 U^2 - \sigma_{rr_0}, \tag{6b}$$

$$\begin{aligned}\rho(U - u)\left[e + \frac{1}{2}(U - u)^2\right] - \sigma_{rr}(U - u)\\ = \rho_0 U\left(e_0 + \frac{1}{2}U^2\right) - \sigma_{rr_0} U,\end{aligned} \tag{6c}$$

$$f_{rr}(U - u) = U, \tag{6d}$$

which relate the state immediately behind the shock ($r = R^+$) to the unshocked quiescent state '0'. These conditions can be reformulated as

$$J = \frac{1}{f_{rr}}, \tag{7a}$$

$$u = a_0(1 - J)M, \tag{7b}$$

$$\sigma_{rr} = \sigma_{rr_0} - \rho_0 a_0^2(1 - J)M^2, \tag{7c}$$

$$e = e_0 - \frac{\sigma_{rr_0}}{\rho_0}(1 - J) + \frac{1}{2}a_0^2\,(1 - J)^2\,M^2, \tag{7d}$$

where $M = U/a_0 > 1$. Observe that $J < 1$ since the material is being compressed by the shock, and that Eq. (4) and (7a) imply that $f_{\theta\theta}$ is unaltered by the shock. We now test different constitutive laws.

D. Neo-Hookean isothermal constitutive law

Assuming an isothermal constitutive law, i.e. e independent of ς, reduces the governing equations to Eq. (1a), (1b) and (5), with the jump conditions to (7a), (7b) and (7c), since the energy equation is now redundant. A fairly general isothermal constitutive law proposed by Blatz and Ko [19] is:

$$e(\boldsymbol{f}) = \frac{\mu}{2\rho_0}(I_1 - 3I_3^{1/3}) + \int_{\rho_0}^{\rho} \frac{p(\rho')}{\rho'^2}\,d\rho', \tag{8}$$

with the density constraint $I_3 = J^2 = (\rho_0/\rho)^2$,where μ is the shear modulus and the so-called hydrostatic pressure p was assumed to not depend on ς. Using the geometrical simplifications of the inverse deformation tensor described in Section II A and transforming both inverse deformation tensor $\boldsymbol{f}$ and stress tensor σ to curvilinear coordinates, we obtain:

$$\sigma_{rr} = \frac{\mu}{J}\left(\frac{1}{f_{rr}^2} - J^{2/3}\right) - p(\rho_0/J), \tag{9a}$$

$$\sigma_{\theta\theta} = \frac{\mu}{J}\left(J^{4-s} f_{rr}^{4-s} - J^{2/3}\right) - p(\rho_0/J). \tag{9b}$$

Unlike gases, the sound speed a in solids depends on the deformation mode: for general three-dimensional deformations, compression (or longitudinal) waves and shear deformation waves exist, each propagating at a different velocity. In radially symmetric motion, the eigenstructure of an hyper-elastic material only involves compression waves traveling at speeds $u \pm a$ with a referring to the longitudinal sound speed, now simply called 'sound speed'. For the isothermal constitutive law (8), we obtain:

$$a = \sqrt{a_\mu^2\left(\frac{1}{f_{rr}^2} + \frac{1}{3}J^{2/3}\right) - \frac{J^2}{\rho_0}\frac{\mathrm{d}p}{\mathrm{d}J}}, \tag{10}$$

where the shear modulus-based wave speed has been defined by $a_\mu \equiv \sqrt{\mu/\rho_0}$.

The derivation of the equation for the $u + a$-characteristic curve and the application of the necessary shock jump conditions are described in Appendix A 1 a and lead to the following ODE for any isothermal pressure form:

$$\frac{\mathrm{d}R}{R} = -\frac{1}{s-1}\frac{a\left[a + a_0(1-J)M\right]\left[-a/J + a_0(1-J)M'(J) - a_0 M\right]}{(1-J)\left[a_0\left(a^2 - 2a_\mu^2 J^2\right)M + a_\mu^2 a(1+J)\right]}\mathrm{d}J, \tag{11a}$$

$$M(J) = \frac{1}{a_0}\sqrt{\frac{1}{1-J}\left[\frac{p(\rho_0/J)}{\rho_0} - a_\mu^2\left(J - J^{-1/3}\right)\right]}, \tag{11b}$$

where $a(J)$ is given by Eq. (10) using Eq. (7a). This ODE can be integrated to obtain R as a function of J

$$\frac{R}{R_i} = \exp\left(-\frac{1}{s-1}\int_{J_i}^{J}\frac{a\left[a + a_0(1-J)M\right]\left[-a/J + a_0(1-J)M'(J) - a_0 M\right]}{(1-J)\left[a_0\left(a^2 - 2a_\mu^2 J^2\right)M + a_\mu^2 a(1+J)\right]}\mathrm{d}J\right), \tag{12}$$

with J_i and R_i the initial density ratio and position of the shock. The shock velocity $U = a_0 M$ is then found using Eq. (11b), and integrated to obtain the shock trajectory $r = R(t)$.

1. *Polynomial dependence for $p(\rho)$*

As an example, we use the pressure form proposed by Miller & Colella in [20] for the Wilkins' flying aluminum plate problem:

$$p\left(\frac{\rho_0}{J}\right) = \sum_{\alpha=1}^{3} c_\alpha\left(\frac{1}{J} - 1\right)^\alpha, \tag{13}$$

where $\mu = 27.8\,\mathrm{GPa}$, $\rho_0 = 2.7\,\mathrm{kg.m^{-3}}$, $c_1 = 72\,\mathrm{GPa}$, $c_2 = 172\,\mathrm{GPa}$, and $c_3 = 40\,\mathrm{GPa}$. In the strong-shock limit $M \gg 1$, (11b) and (13) imply that J must tend to 0, which leads to an infinite density at $r = 0$. A more general power law $p = c_\alpha J^{-\alpha}$ with $\alpha > 1$, similar to the one given by (13) as $M \gg 1$, would simplify the ODE (11) to:

$$\frac{\mathrm{d}R}{R} \simeq \frac{\sqrt{\alpha}}{2(s-1)}\frac{\mathrm{d}J}{J^{3/2}}. \tag{14}$$

Solving Eq. (14), and using Eq. (7b) and (11b), the strong-shock limit gives, for a shock at $r = R$,

$$J \simeq \left(a_0\frac{\rho_0}{c_\alpha}\right)^{-2/\alpha} M^{-2/\alpha}, \tag{15a}$$

$$u \simeq a_0\, M, \tag{15b}$$

$$p \simeq \rho_0 a_0^2\, M^2, \tag{15c}$$

$$a \simeq \sqrt{\frac{\alpha c_\alpha}{\rho_0}}\left(\frac{\rho_0 a_0^2}{c_\alpha}\right)^{(\alpha-1)/2\alpha} M^{(\alpha-1)/\alpha}, \tag{15d}$$

$$\text{with} \quad M \simeq \frac{1}{a_0}\sqrt{\frac{c_\alpha}{\rho_0}}\left[\left(\frac{s-1}{\sqrt{\alpha}}\right)\log\left(\frac{R_i}{R}\right)\right]^\alpha . \tag{15e}$$

It is interesting to notice that the power of $\log(1/R)$ does not depend on the space index. Also observe that for a pressure dependence $p = J^{-\alpha}$, the isentropic exponent defined by $\Gamma \equiv \partial \log p / \partial \log \rho$ is exactly equal to α.

As depicted in Fig. 1(a), the density ratio immediately behind the converging shock predicted by WSD compares favorably with the one obtained from high-resolution numerical simulations, even when the shock is weak. The $u+a$-characteristics obtained from the numerical simulation and the shock trajectory predicted by WSD are displayed in Fig. 1(b). The characteristics behind the shock follow a trajectory that is closer to that of the shock as we approach the origin and the shock becomes stronger, confirming the underlying intuition behind WSD: only a small envelope of information carried by the $u+a$-characteristics can reach the shock, and as the shock strengthens, it has almost lost memory of the flow behind it. Figure 1(c) represents the shock Mach number M as a function of the shock location $R(t)/R_i$, down to dimensionless radii of 10^{-4}. The numerical simulation shows good agreement for low Mach numbers and small discrepancy arises at moderate Mach numbers ($2 \lesssim M \lesssim 5$). At higher Mach numbers, the slope $\mathrm{d}M/\mathrm{d}R$ of both methods agree well until the shock has reached such small radii that the resolution of the computational grid is not sufficient to track the shock, which occurs at $M \approx 50$. As a reference for later comparison with the other constitutive laws tested, we indicate that at $R/R_i = 10^{-1}, 10^{-2}$ and 10^{-3}, the shock Mach numbers obtained in the simulation are $M \approx 2.00$, 5.23 and 16.49 respectively.

2. *Arctanh form for $p(\rho)$*

We investigate an alternate pressure term for the constitutive law defined by Eq. (8):

$$p\left(\frac{\rho_0}{J}\right) = p_0 \left(\frac{\mathrm{Arctanh}\,(J_\infty/J)}{\mathrm{Arctanh}\,(J_\infty)}\right)^\beta, \tag{16}$$

where p_0 is the unshocked pressure and β a positive integer. The material cannot be compressed more than a limit value J_∞ reached at the axis/origin which corresponds to infinite pressure. In contrast, for the same situation, the internal energy and density were unbounded for the polynomial pressure form (13). As J approaches J_∞, $p \sim (-\log(J - J_\infty))^\beta$, and we can show that (11) simplifies to

$$\frac{\mathrm{d}R}{R} \simeq -\frac{1}{s-1}\frac{\mathrm{d}M}{M}. \tag{17}$$

As a result, the strong-shock limit $M \gg 1$ for a shock at $r = R$ gives

$$\begin{aligned} J - J_\infty &\propto e^{-2\psi M^{2/\beta}}, && (18a)\\ u &\propto M, && (18b)\\ p &\propto M^2, && (18c)\\ a &\propto M^{(\beta-1)/\beta} e^{\psi M^{2/\beta}}, && (18d)\\ \text{with } M &\propto R^{-(s-1)}, && (18e) \end{aligned}$$

where $\psi(J_\infty, a_\mu, p_0, \beta)$ is a positive coefficient. From (18e), the shock trajectory near the center follows $R \propto (t_\infty - t)^{1/s}$, where t_∞ defines the implosion time. The exponent in (18e) depends on the space index s only, not on the material properties or other parameters such as J_∞. We also report that the isentropic exponent Γ is not constant, precisely $\Gamma \propto e^{2\psi M^{2/\beta}}/M^{2/\beta}$ as $M \gg 1$.

Figure 2 shows numerical results superposed with the WSD solution. For low values of the integer $\beta = 1$ in (16), J approaches J_∞ at a very small rate $\mathrm{d}J/\mathrm{d}R$ as $r \to 0$, and numerical inconsistencies ultimately arise when the Arctanh argument becomes greater than 1 due to machine precision-generated errors. This is corrected by choosing higher values of β, for example $\beta = 5$ in the present case. As seen in Fig. 2(c), the WSD solution obtained using the Arctanh law for the pressure does not perform as well as polynomial one because the strong-shock regime described by Eq. (18) (where WSD errors are expected to be minimal) is only reached for very small values of $J - J_\infty$ as second-order terms are close to the dominant terms (this can be appreciated in the figure as the power law is not reached for the WSD result until $R/R_i < 2 \cdot 10^{-4}$). We report that $M \approx 2.23$, 8.29 and 43.27 at $R/R_i = 10^{-1}, 10^{-2}$ and 10^{-3} respectively. For a given shock position, the Mach number of the shock is higher than when using a polynomial pressure form, essentially because of the large value of the exponent β chosen and the higher rate of increment of the Mach number with the radius.

E. Neo-Hookean non-isothermal constitutive law

Consider now the following simple non-isothermal constitutive law, to account for high-pressure effects near the axis/origin:

$$e(\boldsymbol{f}, \varsigma) = \frac{\mu}{2\rho_0} I_1 + c_v T_0 J^{1-\gamma} \mathrm{exp}\left(\frac{\varsigma - \varsigma_0}{c_v}\right), \tag{19}$$

where ρ_0, T_0 and ς_0 refer to the unshocked density, temperature and specific entropy, and c_v and γ are the specific heat at constant volume and specific heat ratio. The first part of this constitutive law represents the elastic shear deformation of the material, while the second part simply portrays the internal energy of an ideal gas. We expect this material to behave like an ideal gas in the strong-shock limit (where the pressure term should be dominant) or as $\mu = 0$. The stress components σ_{rr} and $\sigma_{\theta\theta}$ are given by

$$\sigma_{rr} = \frac{\mu}{J f_{rr}^2} - \frac{(\gamma-1)\rho_0}{J}\left\{e - \frac{\mu}{2\rho_0}\left[\frac{1}{f_{rr}^2} + (s-1) J^{4-s} f_{rr}^{4-s}\right]\right\}, \tag{20a}$$

$$\sigma_{\theta\theta} = \mu J^{3-s} f_{rr}^{4-s} - \frac{(\gamma-1)\rho_0}{J}\left\{e - \frac{\mu}{2\rho_0}\left[\frac{1}{f_{rr}^2} + (s-1) J^{4-s} f_{rr}^{4-s}\right]\right\}, \tag{20b}$$

and the sound speed reduces to:

$$a = \sqrt{-\frac{\gamma J \sigma_{rr}}{\rho_0} + (1+\gamma)\frac{a_\mu^2}{f_{rr}^2}}. \tag{21}$$

As $\mu = 0$, Eq. (20a) indeed shows that $\sigma_{rr} = -(\gamma - 1)\rho e$, and the ideal gas sound speed $a = \sqrt{\gamma p/\rho}$ is then recovered with the pressure defined by $p = -\sigma_{rr}$.

The derivation of the ODE resulting from WSD theory is more tedious than that of the isothermal constitutive law. The $u+a$-characteristic equation is reported in Appendix A 2. The combination of that expression with the RH jump conditions (7) gives a final ODE of the form $\mathrm{d}R/R = F(J)\mathrm{d}J$, which reduces in the strong-shock limit to

$$\frac{\mathrm{d}R}{R} \simeq -\frac{n(\gamma)}{s-1}\frac{\mathrm{d}M}{M}, \tag{22a}$$

$$\text{with} \quad n(\gamma) = 1 + \frac{2}{\gamma} + \sqrt{\frac{2\gamma}{\gamma-1}}. \tag{22b}$$

Manipulating the jump conditions (7) further and using Eq. (20a), it can also be shown that J must tend to the finite value $J_\infty = (\gamma-1)/(\gamma+1)$ as $M \gg 1$ (similarly to the ideal gas case), and after integration of (22), we obtain for a shock at $r = R(t)$:

$$J - J_\infty \propto M^{-2}, \tag{23a}$$

$$u \propto M, \tag{23b}$$

$$p \propto M^2, \tag{23c}$$

$$a \propto M, \tag{23d}$$

$$\text{with} \quad M \propto R^{-(s-1)/n}. \tag{23e}$$

While γ has a clear physical meaning for ideal gases, it could be expressed in the constitutive law (19) as a function of the maximum compression ratio $1/J_\infty$ that the solid can reach. The scaling law (23e) corresponds exactly to the power law found by Whitham when applying his WSD method to ideal gases [6], and gives an approximate strong-shock trajectory $R \propto (t_\infty - t)^{n/(n+s-1)}$. Observe in particular that the exponent is independent on μ. In other words, in the strong-shock limit, the solid does experience a zero-shear behavior governed by the pressure part of the constitutive law (19). Moreover, $\Gamma \simeq \gamma$ only as $M \gg 1$, while $\Gamma = \gamma$ for an ideal gas independently of the conditions of compression.

The WSD prediction conforms to the numerical results at all the stages of the shock evolution (Fig. 3). This is confirmed by the observation that characteristics behind the shock follow very closely the trajectory of the shock. The shock Mach number plotted as a function of the shock position offers the best of agreement between WSD and numerical results of the three cases studied. At $R/R_i = 10^{-1}, 10^{-2}$ and 10^{-3}, the shock Mach number is $M \approx 3.17$, 7.71 and 19.02 respectively.

III. PLASTIC MOTION

Most materials submitted to sufficiently high stress conditions undergo large strains when small stress increments are additionally applied, and residual deformations remain even when the stresses are removed. This defines the plastic regime. When uniaxial stress conditions are applied to a deformable medium, the transition between the elastic state and the plastic state can be defined by a limit stress, normally called yield stress. For other stress conditions involving more than one component of the stress tensor, more complex yield criteria determine whether a material point is in plastic or elastic state. Yield criteria are usually based on the deviatoric part of the stress tensor since plasticity appears to be an incompressible process and is therefore intimately related to shear deformations. In the present study, as the converging shock processes the solid with an increasing strength, the shocked material is expected to ultimately reach its intrinsic yield stress and enter the plastic regime. The results shown in the previous section were therefore only valid for some fictitious material with infinitely large yield stress.

A. Finite-deformation plasticity

To account for plasticity, we first introduce a finite-deformation plasticity framework that complements the elastic theory developed in the previous section. The inverse deformation tensor is decomposed into an elastic deformation and a plastic one: $\boldsymbol{f} = \boldsymbol{f}^p \boldsymbol{f}^e$, where $\boldsymbol{f}^e$ and $\boldsymbol{f}^p$ are the elastic and plastic inverse deformation tensors. To meet the particular geometry constraints of this problem, only the diagonal components of these tensors are non zero once transformed to curvilinear coordinates (as was argued in the elastic case). From the compressibility constraints $J = 1/\det \boldsymbol{f}$ and $J^p = 1/\det \boldsymbol{f}^p = 1$ (no change in volume for the plastic deformation), and because $J = J^e J^p$, we can express the $\theta\theta$- and $\phi\phi$-components of the total, elastic and plastic inverse deformation tensors in spherical geometry as functions of their radial counterpart and J:

$$f_{\theta\theta} = f_{\phi\phi} = \sqrt{\frac{1}{J f_{rr}}}, \tag{24a}$$

$$f_{\theta\theta}^e = f_{\phi\phi}^e = \sqrt{\frac{1}{J f_{rr}^e}}, \tag{24b}$$

$$f_{\theta\theta}^p = f_{\phi\phi}^p = \sqrt{\frac{1}{f_{rr}^p}}, \tag{24c}$$

where f_{rr}^e is related the plastic inverse deformation tensor component by

$$f_{rr}^e = \frac{f_{rr}}{f_{rr}^p}. \tag{25}$$

For a cylindrical problem under plain strain however, no assumption about the components f_{zz}^e and f_{zz}^p other than

$f_{zz} = f^e_{zz} f^p_{zz} = 1$ can simplify the problem in a way that would express the non-radial components in terms of the radial ones. We therefore focus on the spherical geometry for the remaining part of the study.

To pursue the analysis further, consider the compressible neo-Hookean isothermal constitutive law given by Eq. (8). Although the energy equation is redundant, it would need to be included to evaluate the plastic dissipation. Because the internal energy determines the energy stored in the solid that can be released by mean of elastic deformation, Eq. (8) must be written in terms of the elastic deformations (and not their total counterparts):

$$e(\boldsymbol{f}^e) = \frac{\mu}{2\rho_0}(I^e_1 - 3(I^e_3)^{1/3}) + \int_{\rho_0}^{\rho} \frac{p(\rho')}{\rho'^2}\, d\rho', \tag{26}$$

with I^e_1, I^e_2, I^e_3 the invariants of the elastic Cauchy–Green tensor $\mathbf{C}^e = (\boldsymbol{f}^e)^{-T}(\boldsymbol{f}^e)^{-1}$. The stresses are computed from $\sigma = -\rho \boldsymbol{f}^{e^T} \partial e/\partial \boldsymbol{f}^e$:

$$\sigma_{rr} = \frac{\mu}{J}\left(\frac{1}{f^{e^2}_{rr}} - J^{2/3}\right) - p(\rho_0/J), \tag{27a}$$

$$\sigma_{\theta\theta} = \sigma_{\phi\phi} = \frac{\mu}{J}\left(J f^e_{rr} - J^{2/3}\right) - p(\rho_0/J). \tag{27b}$$

In general, the system (1a), (1b), (5) and (27) must be completed by an evolution equation for f^p_{rr}, f^e_{rr} being then computed using Eq. (25). In the following subsection, we are exposing a simpler closure.

B. Perfectly plastic model

For simplicity, we consider the material being processed by the converging shock as elastic–perfectly-plastic. In uniaxial stress, this means that plasticity occurs at a constant stress equal to the yield stress σ_Y (i.e. no incremental stress is needed to achieve larger deformations). For more general stress conditions, this concept is extended to a yield criterion of the form $\sigma_{\text{eff}} = \sigma_Y$, where σ_{eff} is an effective stress function. For example, the von Mises constraint may be expressed as

$$\sigma_{\text{eff}} \equiv \sqrt{\frac{3}{2}\text{tr}\,(\Sigma'^T\Sigma')} = \sigma_Y, \tag{28}$$

where Σ' is the deviatoric part of the Mandel stress tensor $\Sigma = -(\rho_0/\rho)\boldsymbol{f}^{e^{-T}}\sigma \boldsymbol{f}^{e^T}$ [21]. Applying this expression to a diagonal stress tensor $\sigma = \text{diag}(\sigma_{rr}, \sigma_{\theta\theta}, \sigma_{\phi\phi})$ and $\sigma_{\phi\phi} = \sigma_{\theta\theta}$, as the one given by (27),

$$\sigma_Y = J|\sigma_{rr} - \sigma_{\theta\theta}|. \tag{29}$$

For the elastic solution behind a converging shock, we had $\sigma_{rr} - \sigma_{\theta\theta} = \mu\left(J^2 - 1\right)/J < 0$, since $J < 1$. Numerical results (see next subsection) shows that $\sigma_{rr} - \sigma_{\theta\theta} < 0$ in the plastic regime as well. Substituting the stresses by their expressions in terms of the elastic deformations given by Eq. (27), we finally obtain the following implicit dependence of f^e_{rr} on J:

$$\frac{\sigma_Y}{\mu} f^{e^2}_{rr} - J f^{e^3}_{rr} + 1 = 0. \tag{30}$$

This relationship implies that the stresses (27) depend on J only, unlike the stresses for a purely elastic material which also depended on f_{rr}. The system of governing equations for an elastic–perfectly-plastic solid processed by a spherical converging shock then reduces to Eq. (1a), (1b), (27) and (30).

1. Shock dynamics for elastic–perfectly-plastic solids

Derivation of the $u+a$-characteristic equation and utilization of the RH jump conditions (see Appendix A 1 b) leads to the final ODE:

$$\frac{\mathrm{d}R}{R} = -\frac{1}{2}\frac{[a + a_0(1-J)M]\,[-a/J + a_0(1-J)M'(J) - a_0 M]}{[a_0 a(1-J)M + \sigma_Y/\rho_0]}\mathrm{d}J, \tag{31a}$$

$$M(J) = \frac{1}{a_0}\sqrt{\frac{1}{1-J}\left[\frac{p(\rho_0/J)}{\rho_0} - a_\mu^2\left(\frac{1}{J f^{e^2}_{rr}} - J^{-1/3}\right)\right]}, \tag{31b}$$

where f^e_{rr} is a function of J through Eq. (30). Integration of Eq. (31a) gives

$$\frac{R}{R_i} = \exp\left(-\frac{1}{2}\int_{J_i}^{J} \frac{[a + a_0(1-J)M]\,[-a/J + a_0(1-J)M'(J) - a_0 M]}{[a_0 a(1-J)M + \sigma_Y/\rho_0]}\mathrm{d}J\right). \tag{32}$$

For the polynomial law (13), the strong-shock limit corresponds to $J \ll 1$, for which $f^e_{rr} \sim J^{-1} \gg 1$ according to the constraint (30). For the Arctanh law (16), large Mach numbers are obtained when J approaches J_∞, while f^e_{rr} reaches a finite value given by Eq. (30) when $J = J_\infty$. For both isothermal laws, the compression effects are dominant over the shear deformation terms and the strong-shock limits are the same as for the purely elastic case (Eq. (15) and (18)). Comparisons with numerical simulations are provided in the following section.

C. Numerical simulation of elastic–plastic shocks

To gain generality, we implemented a numerical experiment allowing the material behind the shock to be initially elastic and to transition to a plastic regime when processed by a stronger shock. The system of equations (1a), (1b), (5), (25) and (27), which govern the deformation of an elastic–plastic solid following a compressible neo-Hookean isothermal constitutive law, is closed by introducing an equation of evolution of the plastic deformation in the radial direction $F^p_{rr} = 1/f^p_{rr}$, expressed in an Eulerian formalism as

$$\frac{\partial \rho F^p_{rr}}{\partial t} + \frac{\partial \rho u F^p_{rr}}{\partial r} = - \frac{2\rho u F^p_{rr}}{r} + \rho F^p_{rr}\dot{\epsilon}\frac{\sigma_{rr}-\sigma_{\theta\theta}}{|\sigma_{rr}-\sigma_{\theta\theta}|}\left(\frac{J|\sigma_{rr}-\sigma_{\theta\theta}|}{\sigma_Y}\right)^N, \tag{33}$$

where the first term of the right-hand side is a geometric source term accounting for the symmetry of the problem, while the second source term incorporates the plastic model [see 18]. The exponent N is a large positive integer (i.e. $N > 10$) and $\dot{\epsilon}$ is a positive constant that can be assigned freely and symbolizes a reference strain rate. The plastic source term tends to zero rapidly when the effective stress $J|\sigma_{rr} - \sigma_{\theta\theta}|$ is smaller than the yield stress σ_Y (elastic regime) so the plastic deformation F^p_{rr} cannot increase. However, when the effective stress overtakes the yield value, this forcing term transforms F^p_{rr} such that the effective stress is brought back to the yield curve, given here by (30).

In contrast to the geometric source term, an implicit time-stepping method is necessary to handle the numerically stiff plastic source term that intends to modify quasi-instantaneously the plastic deformation to bring it back to the yield curve. The splitting strategy now requires the following steps: First, the homogeneous problem related to the system (1a), (1b), (5) and (33) is solved, then the solution is updated using a 4th-order Runge–Kutta explicit method after inclusion of the geometric source terms. Finally an implicit backward Euler method is employed for the plastic source term.

Figure 4 reveals good agreement between the WSD solution described in Paragraph III B 1 and the numerical simulation for a converging shock in aluminum described by an elastic–plastic material following the isothermal constitutive law (26) and (13). The value of the yield stress is so low that the material processed by the incident shock becomes purely plastic even for weak shock strengths (hence the appelation of 'plastic shock') and no elastic–plastic transition is visible here. It can be shown that this material enters the plastic regime for $J \lesssim 0.98$. Plasticity appears to have a positive effect on the agreement between the WSD and numerical simulations when compared to the purely elastic case for this same constitutive law (Fig. 1). Since plasticity is not dominant at the strong shock limit, this effect should be attributed to better agreement at the medium range of Mach numbers ($2 < M_{shock} < 5$) that is where the small disagreement between WSD and simulations appears in the elastic case. At $R/R_i = 10^{-1}, 10^{-2}$ and 10^{-3}, the shock Mach numbers are $M \approx 1.86$, 4.98 and 15.57 respectively. These values are lower than the ones obtained for the purely elastic case with the same constitutive law, indicating that the shock travels at a slower velocity when a finite yield stress is introduced.

1. *Elastic–plastic transition*

To highlight the elastic–plastic transition for non-weak shock waves, we have artificially increased the yield stress and decreased the value of the coefficients in the pressure form (13). Setting $\sigma_Y = 7\,\mathrm{GPa}$ and $c_\alpha = 1$ GPa for $\alpha = 1, 2, 3$, the new material enters the plastic region at $J \approx 0.85$. As reported in Fig. 5(a), an initially elastic shock converges, and a plastic region forms behind as soon as the yield stress has been reached. As the couple 'elastic precursor–plastic region' converges towards the center, the plastic region becomes steeper and narrower while the elastic precursor keeps a constant strength. When approaching the center further, the elastic precursor disappears and a quasi-discontinuous plastic wave remains.

The elastic–plastic transition described in Fig. 5(a) can be tracked using the Hugoniot curve for the material, expressing the response σ_{eff} for smooth compression (Fig. 6). As the material is compressed along the radial direction, prior to reaching the yield point (segment OA in Fig. 6), the entropy remains constant and the restoring force greatly increases (elastic compression). The onset of plasticity is materialized by a kink in the Hugoniot (point A). During this elastic period, the shock Mach number increases from its initial value (in the case of the simulation, $M_i \approx 1.01$) to the elastic precursor Mach number (in this case, $M^e \approx 1.2$). Beyond the yield point, only a slight increase in normal stress is required to significantly compress the material as most of the additional work is converted to entropy instead of additional restoring stress (segment AB). As a result, for a final compression large enough that the yield point is exceeded, the initial state of the material can be linked to the corresponding final state only by an elastic compression of fixed strength up to the cusp (segment OA) and a plastic compression from the cusp to the final level (segment AB). The increment in the slope of the segment initiated at A as the strength of the shock increases is related to the acceleration of the plastic region. If the total compression is large enough, the initial state can be directly connected to the final compressed state without going through the kink, in which case only a plastic compression occurs (segment OD). The path OAC represents the transition from the elastic–plastic to the purely plastic regime, moment in which the plastic region overtakes the elastic precursor.

There exist differences with the elastic–plastic transition observed in planar geometry (see [22] for a detailed description of planar shocks in solids). In planar geometry (see Fig. 5(b)), a plastic discontinuity of constant strength is directly formed behind the elastic precursor (a discontinuous wave of constant strength as well) if the compression is such that the yield point is reached and that both waves can exist. In this case, the elastic precursor travels faster than the plastic shock. In the converging geometry however, as the compression increases, a plastic wave is ultimately formed with a compact radial extent, strengthens, narrows, accelerates, and ultimately overpasses the elastic precursor near the center.

D. Influence of the shear modulus and plasticity on the shock velocity

In this section, we consider the behavior of three materials: i) a purely elastic material of the aluminum kind, following the isothermal constitutive law (8) and (13); ii) its elastic–plastic equivalent, with $\sigma_Y = 0.29$ GPa; iii) the same material with 'zero-shear' ($\mu = 0$). Previous sections have confirmed that the compression term (as $\mu = 0$) becomes dominant as the shock strengthens, along with results for the converging problem that were obtained considering only the compression part of the stress [10, 11]. Figure 7(a) supports the form (11b): the shear-related deformations ($\mu \neq 0$) accelerate the shock. The existence of a finite yield stress limits this effect, giving results that are closer to the zero-shear material. This is because the existence of the finite yield stress decreases the value of the shear part of the Mach number (second term in the square root of (31b)) through the constraint (30). We have chosen to not make the time dimensionless in this plot since a_0 depends on μ. According to Fig. 7(b), for a shock at a given radial location, a purely elastic material is slightly more compressed than its zero-shear and elastic–plastic equivalents due to a higher shock Mach number at a given position.

IV. CONCLUSION

Exact solutions of Whitham's shock dynamics equations for compressible neo-Hookean elastic–plastic solids were derived. Closed expressions for the shock evolution can be obtained in terms of definite integrals. Results show that this method is a highly accurate tool for studying converging shocks, even when shear deformations and plasticity are considered in addition to the hydrostatic pressure contributions commonly used.

Analysis of the strong-shock limit revealed that the behavior of an elastic–plastic material close to the axis/origin $r = 0$ is highly dependent of the pressure equation that is used. For an isothermal law with $p(\rho)$ of the type $p \propto \rho^\alpha$, with $\alpha > 1$, ρ is unbounded at $r = 0$ and $M \propto (\log(1/R))^\alpha$, where the exponent depends on α but neither on other material properties nor on the geometrical space index s. As the shock converges, its shock strength increases at a slower rate than for the two other equations of state investigated for which the density of the shocked material remains bounded close to the origin: $M \propto R^{-(s-1)}$ for an isothermal law with $p(\rho)$ of the Arctanh type, and $M \propto R^{-(s-1)/n(\gamma)}$ for the non-isothermal 'ideal gas'-like constitutive law. For both cases, the exponent depends on s, but the Arctanh strong-shock limit does not involve the maximum compression ratio ρ_∞/ρ_0 that the material can reach at $r = 0$, unlike the ideal gas-like material where ρ_∞/ρ_0 indirectly appears in $n(\gamma)$. The study of more complex constitutive laws remains open for future research.

We have observed that the existence of shear deformation terms accelerates the shock with respect to the same material with a shear modulus artificially set to zero (i.e. with deformations induced by isotropic stresses only). However, limiting the stresses by a yield value attenuates this effect, reaching a result closer to the zero-shear case. Because weak shocks are usually sufficient to overcome common materials' yield stress and initiate plastic deformations behind them, we therefore conclude that isotropic stresses could be solely considered to describe the state of an elastic–plastic solid processed by converging shocks.

The transition from an elastic to a plastic shock exhibits a complex structure of two compression waves moving at different velocities that falls beyond the capabilities of Whitham's shock dynamics. Numerical simulations showed that the converging geometry modifies the elastic precursor–plastic shock structure usually observed in planar symmetry, making the converging plastic shock travel faster than the elastic precursor.

The present work could serve as a basis for studying more complex initial conditions, where perturbations are added to the radially symmetric flow presently studied. In particular, we plan to analyze the Richtmyer-Meshkov flow that would be generated when an imploding wave impacts an inhomogeneous material or more simply an interface between two different materials (e.g. solid–solid or solid–gas interfaces). Previous publications by the authors already analyzed the Richtmyer–Meshkov flow at an impulsively accelerated planar interface between two elastic incompressible solids [23], obtaining stable behavior of the interface in any conditions, and for gas–gas interfaces in converging geometry [24], which can be unstable.

ACKNOWLEDGMENTS

We thank D. I. Pullin and D. I. Meiron for their useful comments on this manuscript. This Material is based upon work supported by the Department of Energy National Nuclear Security Administration under Award Number DE-FC52-08NA28613.

Appendix A: Method of characteristics and Whitham's shock dynamics

The equations of motion (1) and (5) can be written in the following matrix form,

$$\frac{\partial \mathbf{W}}{\partial t} + \mathbf{A}(\mathbf{W})\frac{\partial \mathbf{W}}{\partial r} = \mathbf{S}, \tag{A1}$$

where

$$\mathbf{W} = \begin{pmatrix} \rho \\ u \\ e \\ f_{rr} \end{pmatrix}, \tag{A2a}$$

$$\mathbf{A} = \begin{pmatrix} u & \rho & 0 & 0 \\ -\frac{1}{\rho}\frac{\partial \sigma_{rr}}{\partial \rho} & u & -\frac{1}{\rho}\frac{\partial \sigma_{rr}}{\partial e} & -\frac{1}{\rho}\frac{\partial \sigma_{rr}}{\partial f_{rr}} \\ 0 & -\frac{\sigma_{rr}}{\rho} & u & 0 \\ 0 & f_{rr} & 0 & u \end{pmatrix}, \tag{A2b}$$

$$\mathbf{S} = \frac{s-1}{r}\begin{pmatrix} -\rho u \\ \frac{(\sigma_{rr}-\sigma_{\theta\theta})}{\rho} \\ \frac{u\sigma_{\theta\theta}}{\rho} \\ 0 \end{pmatrix}. \tag{A2c}$$

$\mathbf{W}$ is called the vector of primitive variables, $\mathbf{S}$ contains the geometric terms in the right-hand side of Eq. (1) and (5), and $\mathbf{A}$ is a matrix whose eigenvalues and eigenvectors define the characteristic equations. We find two repeated eigenvalues u associated to two convective modes (along whom trajectory ς and f_{rr} are conserved), and two distinct eigenvalues $u \pm a$ associated to compression modes. The system (A1) decouples as

$$\mathbf{L}\frac{\partial \mathbf{W}}{\partial \mathbf{t}} + \mathbf{LARL}\frac{\partial \mathbf{W}}{\partial \mathbf{r}} = \mathbf{LS}, \tag{A3}$$

where $\mathbf{L}$ and $\mathbf{R}$ are the matrices whose rows and columns respectively contain the left and right eigenvectors of $\mathbf{A}$.

In the WSD approximation, we choose one of the family of characteristic curves whose slope in the $r-t$ plane is closer to that of the shock wave. If the shock advances with positive radial velocity, the correct family of characteristics to approximate the shock path is the one whose eigenvalue is given by $u+a$. Provided that a constitutive law is prescribed, an ODE that relates the changes in the primitive variables dW_i for an infinitesimal change $\mathrm{d}r$ along this characteristic curve can be written. The dW_i can ultimately be related to the change in one variable, the shock Mach number, using the RH conditions (7). As we will discover, it is easier to use $J=\rho_0/\rho$ instead of M as the natural variable in the problem, and differentiation of J and of the RH conditions (7a,b,d) gives:

$$\mathrm{d}\mathbf{W} = \begin{pmatrix} \mathrm{d}\rho \\ \mathrm{d}u \\ \mathrm{d}e \\ \mathrm{d}f_{rr} \end{pmatrix} = \begin{pmatrix} -\rho_0/J^2 \\ a_0\left[(1-J)M'(J)-M\right] \\ \sigma_{rr_0}/\rho_0 + a_0^2(1-J)M\left[(1-J)M'(J)-M\right] \\ -1/J^2 \end{pmatrix}\mathrm{d}J. \tag{A4}$$

We now apply this method to different constitutive laws.

1. Isothermal constitutive law

a. Elastic motion

As mentioned in Section II D, the energy equation is redundant for the isothermal elastic case. This reduces the system of PDEs to Eq. (1a), (1b) and (5). As a consequence, three simple eigenvalues are found (no more entropy mode traveling with the material velocity): $(\lambda_1, \lambda_2, \lambda_3) = (u-a\,, u\,, u+a)$, where a is the sound speed. For the constitutive law (8), the matrices $\mathbf{A}$, $\mathbf{L}$ and $\mathbf{R}$ reduce to:

$$\mathbf{A}=\begin{pmatrix} u & \rho & 0 \\ -\dfrac{1}{\rho}\dfrac{\partial\sigma_{rr}}{\partial\rho} & u & -\dfrac{1}{\rho}\dfrac{\partial\sigma_{rr}}{\partial f_{rr}} \\ 0 & f_{rr} & u \end{pmatrix},\mathbf{L}=\begin{pmatrix} \dfrac{a^2-2a_\mu^2/f_{rr}^2}{\rho a^2} & -\dfrac{1}{a} & \dfrac{2a_\mu^2}{f_{rr}^2 a^2} \\ \dfrac{f_{rr}}{\rho a^2} & 0 & -\dfrac{1}{a^2} \\ \dfrac{a^2-2a_\mu^2/f_{rr}^2}{\rho a^2} & \dfrac{1}{a} & \dfrac{2a_\mu^2}{f_{rr}^2 a^2} \end{pmatrix},\mathbf{R}=\begin{pmatrix} \rho & \dfrac{2a_\mu^2\rho}{f_{rr}^3} & \rho \\ -a & 0 & a \\ f_{rr} & \dfrac{2a_\mu^2}{f_{rr}^2}-a^2 & f_{rr} \end{pmatrix}, \tag{A5a,b,c}$$

where the partial derivatives of σ_{rr} are given by:

$$\frac{1}{\rho}\frac{\partial\sigma_{rr}}{\partial\rho}=\frac{1}{\rho}\left\{a_\mu^2\left[\frac{1}{f_{rr}^2}-\frac{1}{3}\left(\frac{\rho_0}{\rho}\right)^{2/3}\right]-\frac{\mathrm{d}p}{\mathrm{d}\rho}\right\}, \tag{A6a}$$

$$\frac{1}{\rho}\frac{\partial\sigma_{rr}}{\partial f_{rr}}=-\frac{2a_\mu^2}{f_{rr}^3}. \tag{A6b}$$

In the above expressions, the sound speed a is expressed as

$$a=\sqrt{a_\mu^2\left[\frac{1}{f_{rr}^2}+\frac{1}{3}\left(\frac{\rho_0}{\rho}\right)^{2/3}\right]+\frac{\mathrm{d}p}{\mathrm{d}\rho}}. \tag{A7}$$

The characteristic equation corresponding to $\lambda_3=u+a$ reads:

$$\frac{a^2-a_\mu^2/f_{rr}^2}{a^2\rho}\frac{\mathrm{d}\rho}{\mathrm{d}r}+\frac{1}{a}\frac{\mathrm{d}u}{\mathrm{d}r}+\frac{2a_\mu^2}{f_{rr}^2a^2}\frac{\mathrm{d}f_{rr}}{\mathrm{d}r}=\frac{s-1}{\rho a(u+a)r}\left[-\left(a^2-\frac{2a_\mu^2}{f_{rr}^2}\right)\frac{\rho u}{a}+\sigma_{rr}-\sigma_{\theta\theta}\right], \tag{A8}$$

and using Eq. (9) and (A4), and the fact that $r=R(t)$ at the shock location, leads to the ODE

$$\frac{\mathrm{d}R}{R}=-\frac{1}{s-1}\frac{a\left[a+a_0(1-J)M\right]\left[-a/J+a_0(1-J)M'(J)-a_0M\right]}{(1-J)\left[a_0\left(a^2-2a_\mu^2J^2\right)M+a_\mu^2a(1+J)\right]}\mathrm{d}J, \tag{A9a}$$

$$M(J)=\frac{1}{a_0}\sqrt{\frac{1}{1-J}\left[\frac{p(\rho_0/J)}{\rho_0}-a_\mu^2\left(J-J^{-1/3}\right)\right]}, \tag{A9b}$$

for any isothermal pressure form $p(\rho)$.

b. *Perfectly plastic motion*

The existence of a finite yield stress eliminates the explicit dependency of the radial stress with respect to f_{rr}. In contrast, σ_{rr} depends on the density both explicitly through J and through f_{rr}^e by Eq. (30). Three distinct eigenvalues are obtained: $(\lambda_1,\lambda_2,\lambda_3)=(u-a\,,u\,,u+a)$, with the sound speed being:

$$a=\sqrt{-\frac{\mathrm{d}\sigma_{rr}}{\mathrm{d}\rho}}=\sqrt{-a_\mu^2\left(\frac{1}{f_{rr}^{e^2}}+\frac{2}{f_{rr}^{e^3}}\frac{\mathrm{d}f_{rr}^e}{\mathrm{d}J}J-\frac{1}{3}J^{2/3}\right)+\frac{\mathrm{d}p}{\mathrm{d}\rho}}, \tag{A10}$$

with $J=(\rho_0/\rho)$, where the derivative of the elastic deformation with respect to the density ratio can be obtained by differentiating Eq. (30):

$$\frac{\mathrm{d}f_{rr}^e}{\mathrm{d}J}=\frac{f_{rr}^{e^3}}{2f_{rr}^e\sigma_Y/\mu-3Jf_{rr}^{e^2}}. \tag{A11}$$

Then, the matrices $\mathbf{A}$,$\mathbf{L}$ and $\mathbf{R}$ read:

$$\mathbf{A}=\begin{pmatrix} u & \rho & 0 \\ -\frac{1}{\rho}\frac{\partial\sigma_{rr}}{\partial\rho} & u & 0 \\ 0 & f_{rr} & u \end{pmatrix},\ \mathbf{L}=\begin{pmatrix} \frac{f_{rr}}{2\rho} & -\frac{f_{rr}}{2a} & 0 \\ -\frac{f_{rr}}{\rho} & 0 & 1 \\ \frac{f_{rr}}{2\rho} & \frac{f_{rr}}{2a} & 0 \end{pmatrix},\ \mathbf{R}=\begin{pmatrix} \frac{\rho}{f_{rr}} & 0 & \frac{\rho}{f_{rr}} \\ -\frac{a}{f_{rr}} & 0 & \frac{a}{f_{rr}} \\ 1 & 1 & 1 \end{pmatrix}. \tag{A12a,b,c}$$

After finding the left and right eigenvectors, the following ODE holds along the characteristic $\lambda_3 = u + a$:

$$\frac{1}{\rho}\frac{\mathrm{d}\rho}{\mathrm{d}r}+\frac{1}{a}\frac{\mathrm{d}u}{\mathrm{d}r}=\frac{2}{(u+a)r}\left(-\frac{\sigma_Y}{\rho_0 a}-u\right). \tag{A13}$$

Using the RH conditions finally leads to:

$$\frac{\mathrm{d}R}{R}=-\frac{1}{2}\frac{[a+a_0(1-J)M]\,[-a/J+a_0(1-J)M'(J)-a_0M]}{[a_0a(1-J)M+\sigma_Y/\rho_0]}\mathrm{d}J, \tag{A14a}$$

$$M(J)=\frac{1}{a_0}\sqrt{\frac{1}{1-J}\left[\frac{p(\rho_0/J)}{\rho_0}-a_\mu^2\left(\frac{1}{Jf_{rr}^{e2}}-J^{-1/3}\right)\right]}, \tag{A14b}$$

where f^e_{rr} is implicitly given by (30).

2. Non-isothermal constitutive law for elastic motion

In this case, we solve the complete system of equations given by Eq. (1) and (5). Two simple eigenvalues and one eigenvalue of multiplicity two are found: $(\lambda_1, \lambda_2^{(2)}, \lambda_3) = (u-a\,, u\,, u+a)$, with the speed of sound being:

$$a=\sqrt{-\frac{\gamma\sigma_{rr}}{\rho}+\frac{a_\mu^2}{f_{rr}^2}(1+\gamma)}, \tag{A15}$$

where σ_{rr} is given by Eq. (20a). The matrices **A**, **L** and **R** are:

$$\mathbf{A}=\begin{pmatrix} u & \rho & 0 & 0 \\ -\frac{1}{\rho}\frac{\partial\sigma_{rr}}{\partial\rho} & u & -\frac{1}{\rho}\frac{\partial\sigma_{rr}}{\partial e} & -\frac{1}{\rho}\frac{\partial\sigma_{rr}}{\partial f_{rr}} \\ 0 & -\frac{\sigma_{rr}}{\rho} & u & 0 \\ 0 & f_{rr} & 0 & u \end{pmatrix}, \tag{A16a}$$

$$\mathbf{L}=\begin{pmatrix} -\frac{f_{rr}}{2\rho a^2}\frac{\partial\sigma_{rr}}{\partial\rho} & -\frac{f_{rr}}{2a} & -\frac{f_{rr}}{2\rho a^2}\frac{\partial\sigma_{rr}}{\partial e} & -\frac{f_{rr}}{2\rho a^2}\frac{\partial\sigma_{rr}}{\partial f_{rr}} \\ \frac{f_{rr}}{\rho a^2}\frac{\partial\sigma_{rr}}{\partial\rho} & 0 & \frac{f_{rr}}{\rho a^2}\frac{\partial\sigma_{rr}}{\partial e} & \frac{1}{\rho^2a^2}\left(\sigma_{rr}\frac{\partial\sigma_{rr}}{\partial e}-\rho^2\frac{\partial\sigma_{rr}}{\partial\rho}\right) \\ -\frac{\sigma_{rr}}{\rho^2a^2}\frac{\partial\sigma_{rr}}{\partial\rho} & 0 & -\frac{1}{\rho a^2}\left(f_{rr}\frac{\partial\sigma_{rr}}{\partial f_{rr}}+\rho\frac{\partial\sigma_{rr}}{\partial\rho}\right) & -\frac{\sigma_{rr}}{\rho^2a^2}\frac{\partial\sigma_{rr}}{\partial f_{rr}} \\ -\frac{f_{rr}}{2\rho a^2}\frac{\partial\sigma_{rr}}{\partial\rho} & \frac{f_{rr}}{2a} & -\frac{f_{rr}}{2\rho a^2}\frac{\partial\sigma_{rr}}{\partial e} & -\frac{f_{rr}}{2\rho a^2}\frac{\partial\sigma_{rr}}{\partial f_{rr}} \end{pmatrix}, \tag{A16b}$$

$$\mathbf{R}=\begin{pmatrix} \frac{\rho}{f_{rr}} & -\frac{\partial\sigma_{rr}}{\partial f_{rr}}\Big/\frac{\partial\sigma_{rr}}{\partial\rho} & -\frac{\partial\sigma_{rr}}{\partial e}\Big/\frac{\partial\sigma_{rr}}{\partial\rho} & \frac{\rho}{f_{rr}} \\ -\frac{a}{f_{rr}} & 0 & 0 & \frac{a}{f_{rr}} \\ -\frac{\sigma_{rr}}{f_{rr}\rho} & 0 & 1 & -\frac{\sigma_{rr}}{f_{rr}\rho} \\ 1 & 1 & 0 & 1 \end{pmatrix}, \tag{A16c}$$

where the partial derivatives of the radial stress are computed as follow:

$$\frac{\partial \sigma_{rr}}{\partial \rho} = \frac{2J\sigma_{rr} - \mu(\gamma-1)(s-1)(4-s)J^{4-s}f_{rr}^{4-s}}{2\rho_0}, \tag{A17a}$$

$$\frac{\partial \sigma_{rr}}{\partial e} = -\frac{(\gamma-1)\rho_0}{J}, \tag{A17b}$$

$$\frac{\partial \sigma_{rr}}{\partial f_{rr}} = \frac{\mu}{J}\left[-\frac{\gamma+1}{f_{rr}^3} + \frac{(\gamma-1)(s-1)(4-s)J^{4-s}f_{rr}^{3-s}}{2}\right]. \tag{A17c}$$

The characteristic equation corresponding to $\lambda_4 = u + a$ can be written as:

$$\mathbf{L}_{4,:}\frac{\mathrm{d}\mathbf{W}}{\mathrm{d}r} = \frac{1}{u+a}\mathbf{L}_{4,:}\mathbf{S}, \tag{A18}$$

where $\mathbf{L}_{4,:}$ is the fourth row of matrix (A16b). Noting the source term (A2c) as $\mathbf{S} = (s-1)\mathbf{S}'/r$ and using Eq. (7), (20) and (A4), we obtain the closed ODE:

$$\frac{\mathrm{d}R}{R} = \frac{1}{s-1}\frac{[a + a_0(1-J)M]\,\mathbf{L}_{4,:}(J)\mathrm{d}\mathbf{W}/\mathrm{d}J}{\mathbf{L}_{4,:}(J)\mathbf{S}'(J)}\mathrm{d}J, \tag{A19a}$$

$$M(J) = \frac{1}{a_0}\sqrt{\frac{a_\mu^2\left[2 - J^2 - \gamma(J+2)^2\right] + 2e_0(\gamma-1) + 2\sigma_{rr_0}\left[1-\gamma(1-J)\right]/\rho_0}{(1-J)\left[1+J-\gamma(1-J)\right]}}. \tag{A19b}$$

[1] R. Masri and D. Durban. Dynamic spherical cavity expansion in an elastoplastic compressible Mises solid. *Journal of Applied Mechanics*, 72:887–898, 2005.

[2] J. D. Lindl. *Inertial confinement fusion: The quest for ignition and energy gain using indirect drive*. Springer, 1998.

[3] S. Belov, G. Boriskov, A. Bykov, R. Ilkaev, N. Lukyanov, A. Matveev, O. Mikhailova, V. Selemir, G. Simakov, R. Trunin, I. Trusov, V. Urlin, V. Fortov, and A. Shuikin. Shock compression of solid deuterium. *JETP Letters*, 76:433–435, 2002.

[4] P. U. Andersson and L. Holmlid. Ultra-dense deuterium: A possible nuclear fuel for inertial confinement fusion (ICF). *Physics Letters A*, 373(34):3067–3070, 2009.

[5] G. Guderley. Starke Kugelige und zylindrische Verdichtungsstösse in der Nähe des Kugelmittelpunktes bzw der Zylinderachse. *Luftfahrtforschung*, 19:302–312, 1942.

[6] G. B. Whitham. *Linear and Nonlinear Waves*. John Wiley and sons, 1974.

[7] H. G. Hornung, D. I. Pullin, and N. F. Ponchaut. On the question of universality of imploding shock waves. *Acta Mechanica*, 201:31–35, 2008.

[8] G. Ben-Dor. Two dimensional interactions. In G. Ben-Dor, O. Igra, and T. Elperin, editors, *Handbook of shock waves*, volume 2, pages 68–265. Academic Press, 2001.

[9] G. B. Whitham. A new approach to problems of shock dynamics Part I Two-dimensional problems. *Journal of Fluid Mechanics*, 2:145–171, 1957.

[10] H. S. Yadav and V. P. Singh. Converging shock waves in metals. *Pramana*, 18:331–338, 1982.

[11] T. Hiroe, H. Matsuo, and K. Fujiwara. Numerical simulation of cylindrical converging shocks in solids. *Journal of Applied Physics*, 72:2605–2611, 1992.

[12] J. Marsden and T.Hughes. *Mathematical foundations of elasticity*. Dover Publications, 1993.

[13] G. H. Miller and P. Colella. A conservative three-dimensional eulerian method for coupled solid-fluid shock capturing. *Journal of Computational Physics*, 183(1):26 – 82, 2002.

[14] S.L. Gavrilyuk, N. Favrie, and R. Saurel. Modelling wave dynamics of compressible elastic materials. *Journal of Computational Physics*, 227(5):2941 – 2969, 2008.

[15] T.J. Ahrens. Equations of state. In M. Shahinpoor J. R. Asay, editor, *High-Pressure Shock Compression of Solids*, volume 1, pages 75–114. Springer, 1993.

[16] M. Levinson and I.W. Burgess. A comparison of some simple constitutive relations for slightly compressible rubber-like materials. *International Journal of Mechanical Sciences*, 13(6):563 – 572, 1971.

[17] E. F. Toro. *Riemann Solvers and Numerical Methods for Fluid Dynamics*. Springer, 1999.

[18] D. J. Hill, D. I. Pullin, M. Ortiz, and D. I. Meiron. An Eulerian hybrid WENO centered-difference solver for elastic-plastic solids. *Journal of Computational Physics*, 229:9053–9072, 2010.

[19] P. J. Blatz and W. L. Ko. Application of finite elastic theory to the deformation of rubbery materials. *Trans. Soc. Rheology*, 6:223–252, 1962.

[20] G. H. Miller and P. Colella. A high-order Eulerian Godunov method for elastic–plastic flow in solids. *Journal of computational physics*, 167:131–176, 2001.

[21] S. Cleja-Tigoiu and G. Maugin. Eshelby's stress tensors in finite elastoplasticity. *Acta Mechanica*, 139:231–249, 2000.

[22] R. Menikoff. Elastic–plastic shock waves. In Y. Horie, editor, *Shock Wave Science and Technology Reference Library*, volume 2, Solids I, pages 189–224. Springer, 2007.

[23] A. López Ortega, D. J. Hill, D. I. Pullin, and D. I. Meiron. Linearized Richtmyer–Meshkov flow analysis for impulsively accelerated incompressible solids. *Phys. Rev. E*, 81(6):066305, 2010.

[24] M. Lombardini and D. I. Pullin. Small-amplitude perturbations in the three-dimensional cylindrical Richtmyer–Meshkov instability. *Physics of Fluids*, 21(11):114103, 2009.

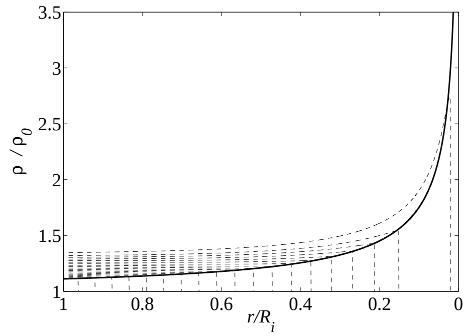

(a)ρ/ρ_0 vs r/R_i.

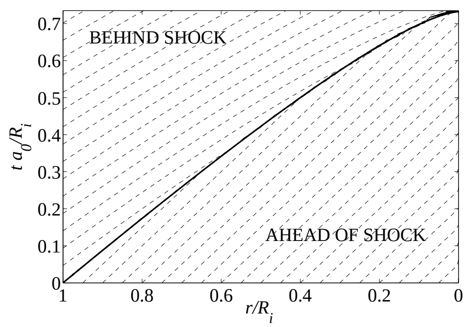

(b)$r - t$ diagram

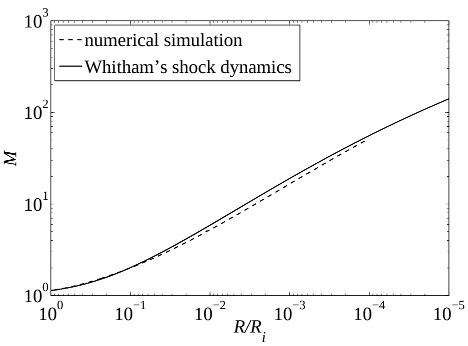

(c)$R/R_i - M$ logarithmic

FIG. 1. Spherically symmetric ($s = 3$) converging shock initially started at $R = R_i$ with $J_i = 0.9$ (i.e. $M_i \approx 1.14$) and propagating from left to right into a purely elastic solid medium described by the isothermal constitutive law (8) with polynomial pressure form (13): (a) Density radial profiles obtained from the numerical simulation at equally spaced times (dashed lines) and density ratio immediately behind the shock ($r = R(t)^+$) given by WSD (solid line); (b) $u + a$-characteristics obtained from numerical simulation (dashed lines) and shock trajectory $r = R(t)$ vs t obtained from WSD (solid line); (c) Shock Mach number M as a function of the shock position $R(t)$ plotted in a log–log scale, from the simulation (dashed line) and WSD (solid line).

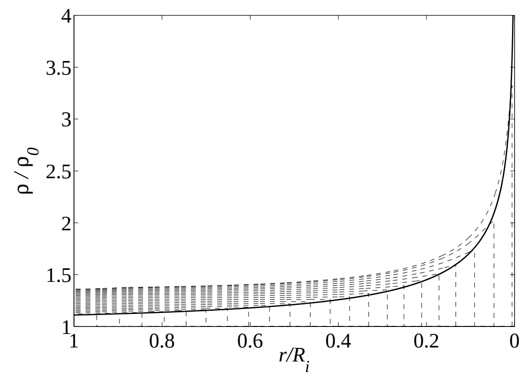

(a)ρ/ρ_0 vs r/R_i.

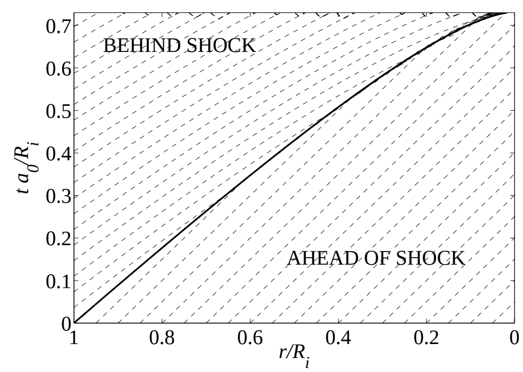

(b)$r - t$ diagram

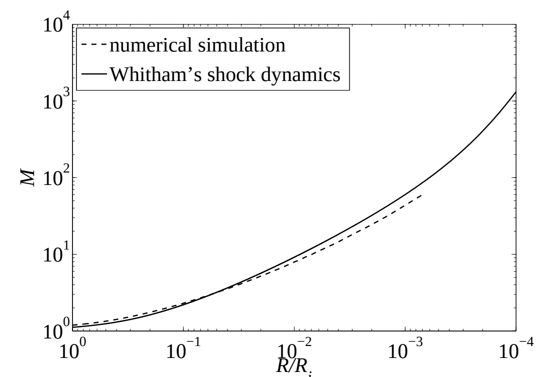

(c)$R/R_i - M$ logarithmic

FIG. 2. Spherically symmetric ($s = 3$) converging shock initially started at $R = R_i$ with $J_i = 0.9$ (i.e. $M_i \approx 1.02$) and propagating from left to right into a purely elastic solid medium described by the isothermal constitutive law (8), using the Arctanh pressure form (16) with the choice $J_\infty = 1/6$, $p_0 = 10\,\mathrm{GPa}$ and $\beta = 5$. See Fig. 1 for keys.

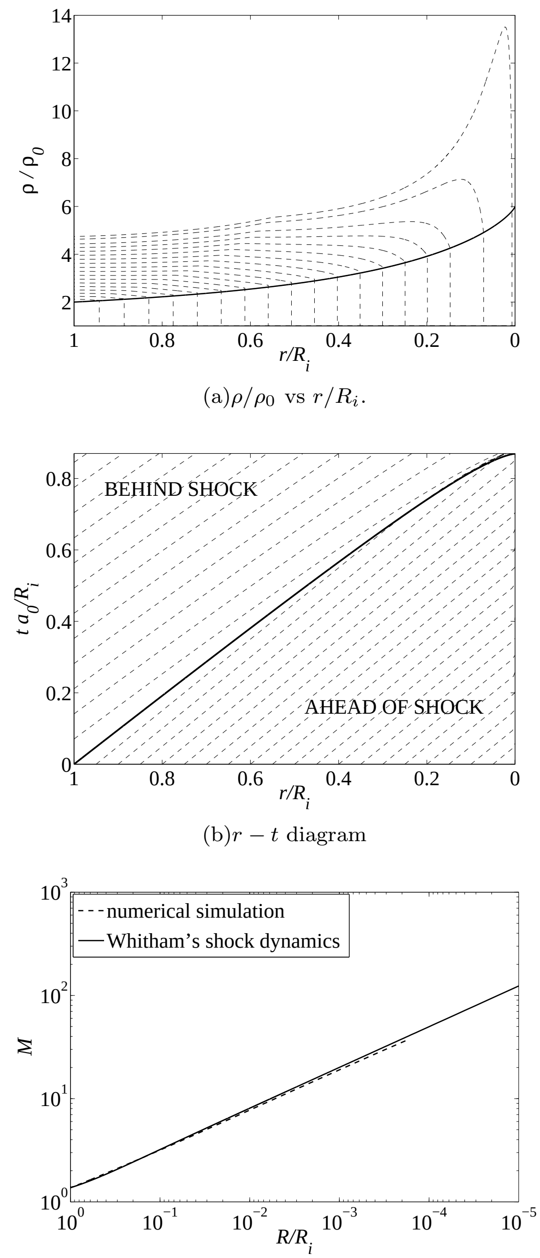

(a)ρ/ρ_0 vs r/R_i.

(b)$r - t$ diagram

(c)$R/R_i - M$ logarithmic

FIG. 3. Spherically symmetric ($s = 3$) converging shock initially started at $R = R_i$ with $J_i = 0.9$ (i.e. $M_i \approx 1.07$) and propagating from left to right into a purely elastic solid medium described by the non-isothermal constitutive law (19) with $\gamma = 1.4$ (i.e. $J_\infty = 1/6$). See Fig. 1 for keys.

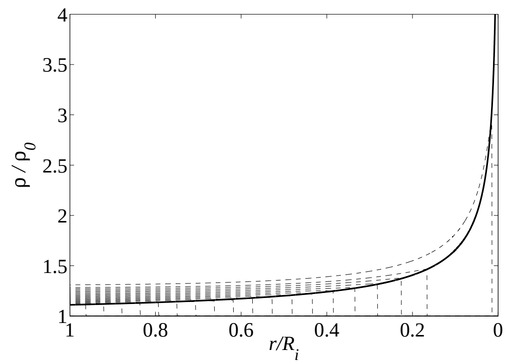

(a)ρ/ρ_0 vs r/R_i for plastic shock

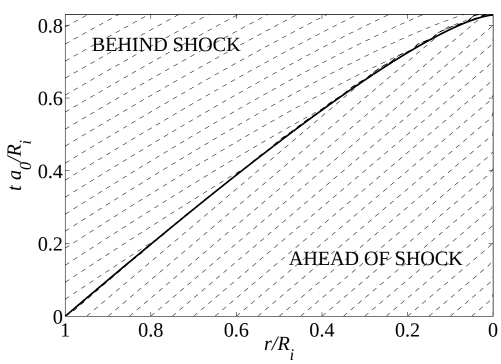

(b)$r - t$ diagram

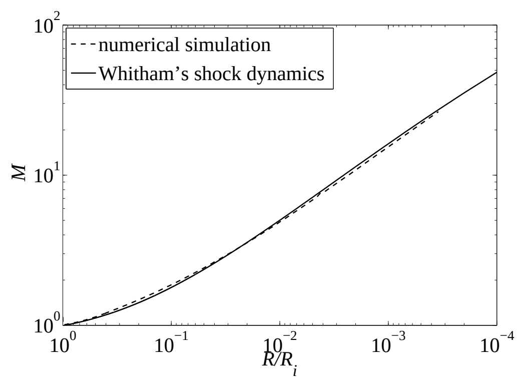

(c)$R/R_i - M$ logarithmic

FIG. 4. Spherically symmetric ($s = 3$) converging shock initially started at $R = R_i$ with $J_i = 0.9$ (i.e. $M_i \approx 1.01$) and propagating from left to right into an elastic–plastic solid medium following the the isothermal constitutive law (26) with the polynomial pressure form (13), and given the von Mises constraint (28) with $\sigma_Y = 0.29$ GPa (aluminum). See Fig. 1 for keys.

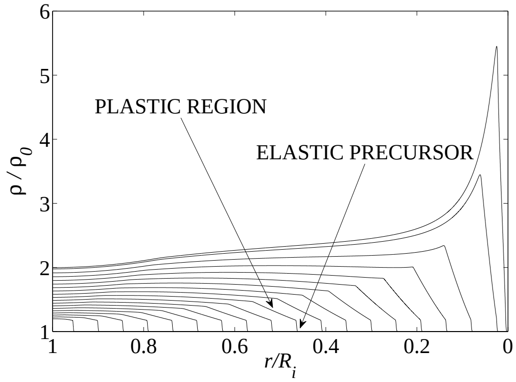

(a)Spherical $s = 3$, $J_i = 0.9$ ($M_i \approx 1.01$)

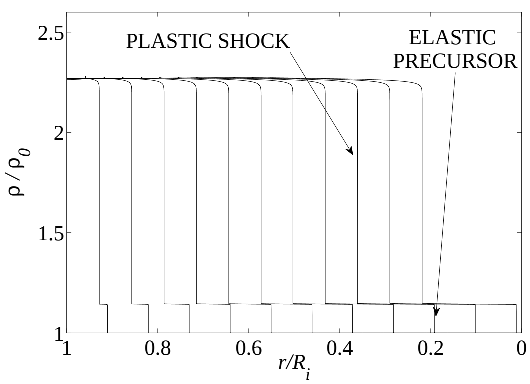

(b)Planar $s = 1$, $J_i = 0.48$

FIG. 5. Density radial profiles obtained from the numerical simulation for (a) spherically symmetric converging and (b) planar motion. Elastic–plastic deformations follow the isothermal constitutive law (26), using the polynomial pressure form (13) with $c_1 = c_2 = c_3 = 1$GPa, and given the von Mises constraint (28) with $\sigma_Y = 7$GPa. Note that for the planar case an initial shock Mach number cannot be defined since the shock is started beyond the elastic–plastic transition. The elastic precursor Mach number is $M^e \approx 1.02$ for both simulations

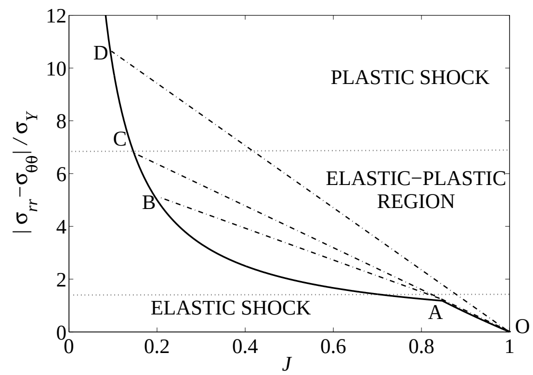

FIG. 6. $|\sigma_{rr} - \sigma_{\theta\theta}|/\sigma_Y$ vs $J(= \rho_0/\rho)$ immediately behind the shock for an elastic–plastic material. The Hugoniot curve (i.e. the locus of the possible post-shock states of the material for a given initial condition) is completed by some Rayleigh lines (i.e. the thermodynamic path connecting the initial state with a post-shock state). Isothermal polynomial pressure form is considered, but the shape of the Hugoniot curve and the different regions can be reproduced for other constitutive laws.

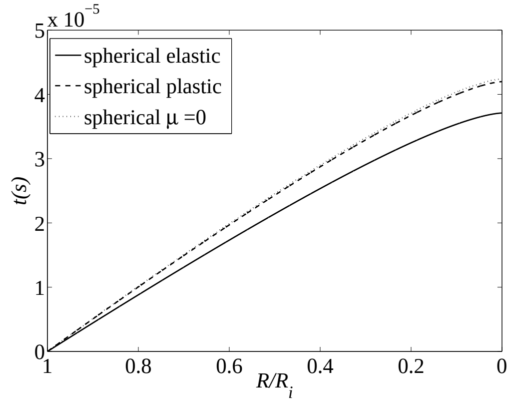

(a)Shock trajectory

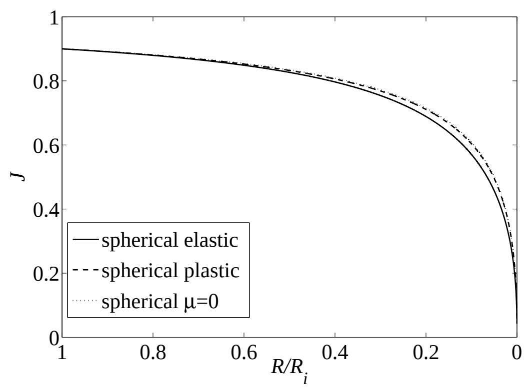

(b)$J(=\rho_0/\rho)$ at $r = R^+$ vs R/R_i

FIG. 7. (a) Shock trajectory and (b) J immediately behind the shock vs R for a spherically symmetric ($s = 3$) converging shock initially stated at $r = R_i$ with $J_i = 0.9$. Comparisons between the purely elastic, elastic–plastic and zero-shear solid simulations using the isothermal constitutive law (8) or (26), with the polynomial pressure form (13). $\sigma_Y = 0.29$ GPa was used for the elastic–plastic case.